Performance Characteristics of a Whole-Body PET Scanner

Timothy R. DeGrado, Timothy G. Turkington, J. Jay Williams, Charles W. Stearns, John M. Hoffman and R. Edward Coleman

Duke University Medical Center, Durham, North Carolina and General Electric Medical Systems, Milwaukee, Wisconsin

Methods: This study characterizes the performance of a newly developed whole-body PET scanner (Advance, General Electric Medical Systems, Milwaukee, WI). The scanner consists of 12,096 bismuth germanate crystals (4.0 mm transaxial by 8.1 mm axial by 30 mm radial) in 18 rings, giving 35 two-dimensional image planes through an axial field of view of 15.2 cm. The rings are separated by retractable tungsten septa. Intrinsic spatial resolution, scatter fraction, sensitivity, high count rate performance and image quality are evaluated. **Results:** Transaxial resolution (in FWHM) is 3.8 mm at the center and increases to 5.0 mm tangential and 7.3 mm radial at R = 20 cm. Average axial resolution decreases from 4.0 mm FWHM at the center to 6.6 mm at R = 20 cm. Scatter fraction is 9.4% and 10.2% for direct and cross slices, respectively. With septa out, the average scatter fraction is 34%. Total system sensitivity for true events (in kcps/(μCi/cc)) is 223 with septa in and 1200 with septa out. Dead-time losses of 50% correspond to a radioactivity concentration of 4.9 (0.81) μCi/cc and a true event count rate of 489 (480) kcps with septa in (out). Noise-equivalent count rate (NECR) for the system as a whole shows a maximum of 261 (159) kcps at a radioactivity concentration of 4.1 (0.65) μCi/cc with septa in (out). NECR is insensitive to changes in lower gamma-energy discrimination between 250–350 keV. **Conclusions:** The results show the performance of the newly designed PET scanner to be well suited for clinical and research applications.

Key Words: PET; instrumentation; performance

J Nucl Med 1994; 35:1398–1406

P ET measures physiological and biochemical processes in vivo through quantitative imaging of positron-emitter labeled molecules in the human body. PET scanners have continued to improve since the initial development of a scanner that had a spatial resolution (FWHM) of approximately 2.5 cm and acquired a single image plane (*1*). The need for improved spatial resolution and a greater axial field of view (FOV) was immediately recognized, and a trend ensued toward smaller detectors and a greater number of image planes (for a review, see ref. 2).

Many current PET scanners utilize crystalline bismuth germanate (BGO) as scintillator material. The short path-length of 511 keV annihilation photons in BGO allows the employment of detector units (or detector blocks) composed of two-dimensional matrices of BGO crystals monitored by a smaller number of photomultiplier tubes (*2*). In recent developments, the axial FOV of BGO-based PET scanners has been increased to ~15 cm to provide more comprehensive imaging of the human brain and heart, and more efficient scanning of the whole body for oncologic applications of PET (*3,4*).

A new BGO-based whole-body PET scanner has been designed for both research and clinical applications with the following guiding criteria: (1) Intrinsic spatial resolution of 4–6 mm FWHM; (2) Capability to remove collimating septa and acquire all axial lines of response for true three-dimensional imaging; (3) High count rate performance; and (4) Axial FOV of 15 cm. The performance of the new system is demonstrated in this report.

MATERIALS AND METHODS

System Description

The newly designed PET scanner (Advance, General Electric Medical Systems, Milwaukee, WI) has 12,096 bismuth germanate (BGO) crystals in 18 rings to detect positron annihilation photons. The crystals have dimensions of 4.0 mm transaxial × 8.1 axial × 30 mm radial and are grouped in detector units of 6 × 6 crystals each. In each detector unit, the crystals are viewed by two dual-photomultiplier tubes (Hamamatsu R1548). Three rings of 112 detector units each form a detector ring of 92.7 cm diameter and 15.2 cm axial length. The detector units are housed in 56 modules of six detector units each (2 transaxial × 3 axial). The detector ring is housed in a gantry which provides a 59-cm diameter patient port. The gantry tilts up to ±20° from vertical for alignment with imaging planes of interest. The imaging field of view (FOV) is 55 cm in diameter by 15.2 cm in axial length. The 18 crystal rings form 35 two-dimensional imaging planes spaced by 4.25 mm. The system has tungsten septa 1 mm thick and 12 cm long. The septa define the image planes in a two-dimensional scanning mode and are automatically retracted for three-dimensional scanning mode. A Hewlett Packard Apollo 9000 Model 735 workstation (Palo Alto, CA) provides control for the system and also serves as an

image display and analysis station. All operations are performed through a graphical user interface (X window system under Motif).

The signals from the detectors undergo amplification and coarse energy threshold discrimination at each detector unit within the gantry. The detector live-time is monitored to allow the application of a dead-time correction technique. The signals are further processed into digital packets containing position and energy information. The position signals are used to localize the active crystal within the detector unit by a two-dimensional position map. The energy signals are used to apply lower and upper gamma-energy discrimination at each crystal. A digital time stamp of 2-nsec resolution is added to each signal. To reduce hardware requirements, signals are multiplexed at the module level (six detector units). The coincidence processing module (5) analyzes all incoming events within processing cycles of a 250-nsec period and is configurable for coincidence timing window width, transaxial and axial FOV, and axial acceptance angle. Prompt and delayed coincidence events may be sorted and stored separately in histogram memory. Alternatively, for realtime randoms correction, the delayed coincidence events are subtracted from the prompts and only the difference is stored. The sorter and histogrammer have a sustained throughput capability of five million coincidence events per second. At the termination of each acquisition frame, the data in histogram memory is transferred to a hard disk.

Dead-time correction is applied to each sinogram element by estimation of live-time of contributing coincidence channels. The live-time estimate of each coincidence channel is the product of (1) the measured live-times of the two coincident detector units; (2) the live-times of the two signal multiplexers; (3) a factor accounting for the coincidence processor packet losses and sorter bandwidth capacity; and (4) an experimentally determined factor to account for other, unmeasured event losses.

For two-dimensional imaging, the data are acquired and processed in one of two different modes according to the axial acceptance angle. As illustrated in Figure 1, sinograms of direct planes acquired in the high-sensitivity mode include not only coincidence events from directly opposing crystals but also those from the two crossing planes of neighboring crystals. In the high-resolution mode, the direct slices include only events from directly opposing crystals. Sinograms for cross planes are similarly derived from events in four crossing planes for the high-sensitivity mode, whereas only the two nearest crossing planes are utilized in the high-resolution mode. The standard acquisition mode in two-dimensional scanning is the high-sensitivity mode. In the three-dimensional mode, all possible lines of response (18 × 18 = 324) may be acquired and stored in a format suitable for subsequent data processing. The data may be acquired as a static frame, a sequence of frames, or binned into dynamic frames using external gating. The minimum duration of a frame is 1 sec. The data transfer rate from histogram memory to the hard disk is ~3 Mbyte/sec.

For acquisition of transmission data, a pair of 10-mCi [68]Ge pin sources are mechanically positioned and rotated about the longitudinal axis of the FOV. A transmission mask is applied to the data (cutoff 6–7) at a width of 9 sinogram elements, providing optimal noise-equivalent count rate (NECR).

Image reconstruction for two-dimensional scanning uses an array processor for the filtered backprojection technique. Hanning, Shepp-Logan and Butterworth windows are available, as well as the ramp filter alone. Reconstruction times (including

data positioning, normalization, scatter correction and attenuation correction) are <2.5 sec per plane for a 128 × 128 pixel image and <4.0 sec for a 256 × 256 pixel image. Image reconstruction software for data acquired in the three-dimensional mode was not available at the time of this study.

Configuration settings for lower and upper gamma-energy discriminator level and coincidence window width may be altered in the software. These settings are fixed in clinical use to ensure the efficacy of data corrections (principally dead-time and scatter).

Performance Measurements

Except where specified otherwise, performance measurements and data processing were performed in accordance with the guidelines provided by the joint committee on PET performance standards of the Society of Nuclear Medicine (SNM) and the National Electronics Manufacturers Association (NEMA) as described by Karp et al. (8). Many of the tests used a fillable, lucite cylinder (20 cm ID, 18.5 cm length) referred to as the performance phantom (8). Standard settings of the coincidence window, lower level gamma-energy discriminator (LLD) and upper level gamma-energy discriminator were 12.5 nsec, 300 keV and 650 keV, respectively. The positron emitter ^{18}F, produced on a CS-30 medical cyclotron, was used in measurements with line sources and phantoms. The ^{18}F was in aqueous soluble form of either ionic fluoride or 2-fluorodeoxyglucose (FDG).
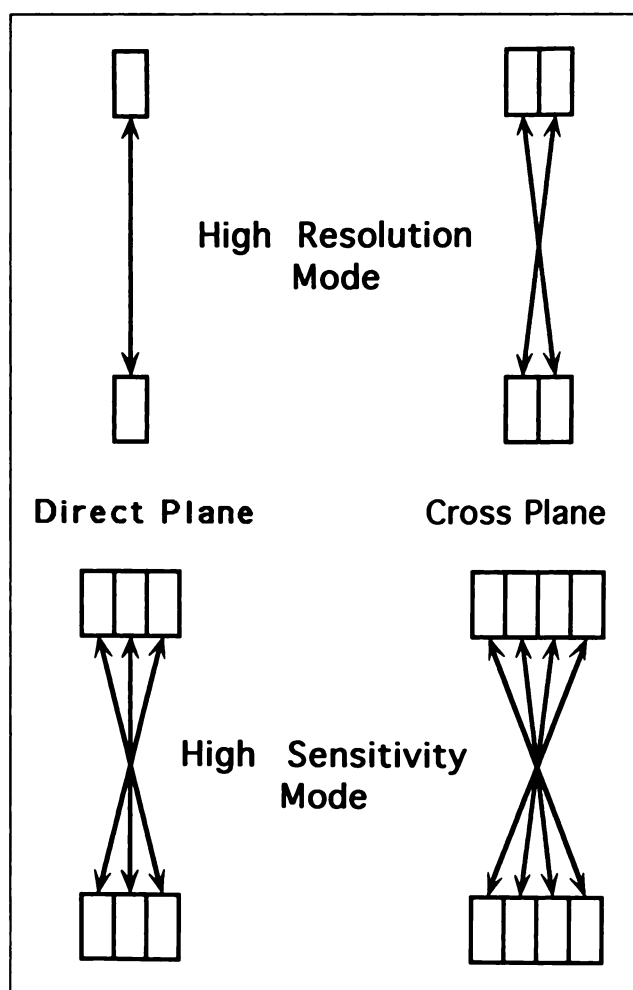

FIGURE 1. Coincidence path acceptance in axial direction for the two modes of two-dimensional imaging with the PET scanner.

Intrinsic Spatial Resolution

Transaxial resolution was measured with a stainless steel needle (1.2 mm ID, 1.65 mm OD) filled with ^{18}F-activity (~0.2 mCi). The line source was placed in air at seven positions with respect to the center of the field of view (R = 0, 1, 2, 5, 10, 15 and 20 cm). Data were acquired in both two-dimensional modes. The data were reconstructed on a 256 × 256 grid with a pixel size of 0.25 mm, using a ramp filter cutoff at the Nyquist frequency (4 mm filter width). Vertical and horizontal profiles through the center of the point images were defined. The FWHM in both radial and tangential directions was determined from these profiles by linear interpolation.

The axial slice profile width was measured by stepping an ^{18}F point source in air at 0.5-mm intervals through the axial FOV. The point source was composed of [18]F (~0.2 mCi) on a 4-mm diameter disk of filter paper sandwiched between two 1-mm thick aluminum disks. Data were acquired at radii R = 0, 10 and 20 cm. For each plane, profiles were obtained (counts versus axial distance) and then normalized to the area under the curve (counts · mm). The FWHM was determined for each plane by linear interpolation.

Scatter

The scatter fraction was determined for an ^{18}F line source (~0.3 mCi) in a water-filled performance phantom. Data were acquired with extended septa in high-resolution and high-sensitivity modes at three LLDs of 250, 300 and 350 keV. Data were also acquired with septa out at each of the three LLDs and a factor of five lower in activity in the line source. The line source was positioned at three radii, 0, 4 and 8 cm, in order to determine the average scatter over the whole FOV. A fixed diameter of 24 cm was used for the calculation of scatter. The sinogram profiles were used to calculate the number of scatter events within the FOV, and the number of true events within a 2-cm radius of the source. The scatter within the peak is estimated by assuming a constant background, the level of which was determined by the average of the pixel intensities at the edge of the peak (±2 cm). The average scatter fraction (SF) over the whole area of the phantom was calculated by weighting the data for each position by the area of the annulus at that radius:

$$SF = \frac{[R_s(0) + 8 \cdot R_s(4.0) + 16 \cdot R_s(8.0)]}{[R_{tot}(0) + 8 \cdot R_{tot}(4.0) + 16 \cdot R_{tot}(8.0)]}, \quad \text{Eq. 1}$$

where R_s is the count rate per unit activity of scattered events as a function of radius and R_{tot} is the total count rate per unit activity.

The two-dimensional scatter correction algorithm of Bergström et al. (9) was implemented. The accuracy of this correction was tested using a single nonradioactive water-filled rod insert in the test phantom filled with radioactive water (~1 mCi ^{18}F). The phantom was offset from the center by 25 mm. Images were reconstructed onto a 256 × 256 matrix of 1 mm pixel size using a 4-mm wide ramp filter. Calculated attenuation correction was applied. The averaged pixel value in a 30-mm diameter region of interest (ROI) centered over the nonradioactive insert (where the average pixel value should be zero) is expressed as a percentage of the average pixel value in 11 ROIs of the same size placed in the radioactive background.

Sensitivity

The volume sensitivity of true events was determined by loading the performance phantom with ^{18}F in water at a concentration less than 0.2 μCi/cc. Measurements were performed in both high-

resolution and high-sensitivity modes (septa in) at three LLD settings of 250, 300 and 350 keV. Data were also acquired with septa out at the same thresholds and a factor of eight lower concentration of radioactivity. The count rate was determined from the sinograms corresponding to a 24-cm transverse FOV. For each slice acquired with septa in, the true event sensitivity was calculated as the total sensitivity multiplied by the factor (1-SF). The scatter fractions were determined as described above. The average scatter fraction for direct slices was utilized for the calculation of true sensitivity for direct slices. Similarly, the average cross-slice scatter fraction was used for the calculation of true sensitivity for cross slices. Total system sensitivities were calculated as the sum of all slice sensitivities. Sensitivity in three-dimensional mode was determined by adding all the counts (randoms subtracted) within the 24-cm transverse FOV, and multiplying by (1-SF). The three-dimensional scatter fraction was determined as previously described.

Count Rate Performance

To investigate the count rate performance characteristics of the PET scanner, the performance phantom was filled with ^{18}F activity with an initial concentration of about 16 μCi/cc, centered in the FOV, and scanned repeatedly over a period of 14 hr with septa in. A similar study was performed with the septa out and an initial ^{18}F-activity concentration of about 1.5 μCi/cc. The random coincidence events were simultaneously measured by the delayed coincidence technique. Measurements were performed in both high-resolution and high-sensitivity modes at three LLD settings of 250, 300 and 350 keV. Count rates for true scatter coincidence events ((T + S)$_{meas}$) over the entire transaxial and FOV were utilized to investigate the dead-time characteristics. The percent dead-time (%DT), as a function of concentration of radioactivity, was calculated as:

$$\%DT = 100 \cdot \left(1 - \frac{(T + S)_{meas}}{(T + S)_{extrap}}\right). \quad \text{Eq. 2}$$

The 50% dead-time point was recorded for each slice and for system-averaged count rates. The true coincidence count rate (T) for a 24-cm transaxial FOV was calculated from the true + scatter rate and the appropriate scatter fraction as previously discussed for measurement of sensitivity. The random coincidence event rate was determined also for the 24-cm FOV. The peak of the true event rate and the point at which the true event rate was equal to the random event rate (R) were determined. To investigate the relationship of data acquisition parameters on the signal-to-noise ratio, the noise equivalent count rate (NECR) was calculated as (10):

$$NECR = \frac{T}{\left(1 + \frac{S}{T} + \frac{2R}{T}\right)}. \quad \text{Eq. 3}$$

The term 2R/T in the denominator is appropriate, since randoms correction is performed by delayed event subtraction.

The accuracy of the dead-time correction algorithm was measured in a different acquisition run with the test phantom containing [18]F (~50 mCi) in water. The phantom was dynamically scanned over a 14-hr period. Images were reconstructed on a 128 × 128 pixel grid representing a 25.5-cm diameter FOV with a ramp filter 4 mm wide. Radioactivity concentration was evaluated through the user-interface for circular ROIs of 16.5 cm diameter centered in each plane of each dynamic frame. The percent error
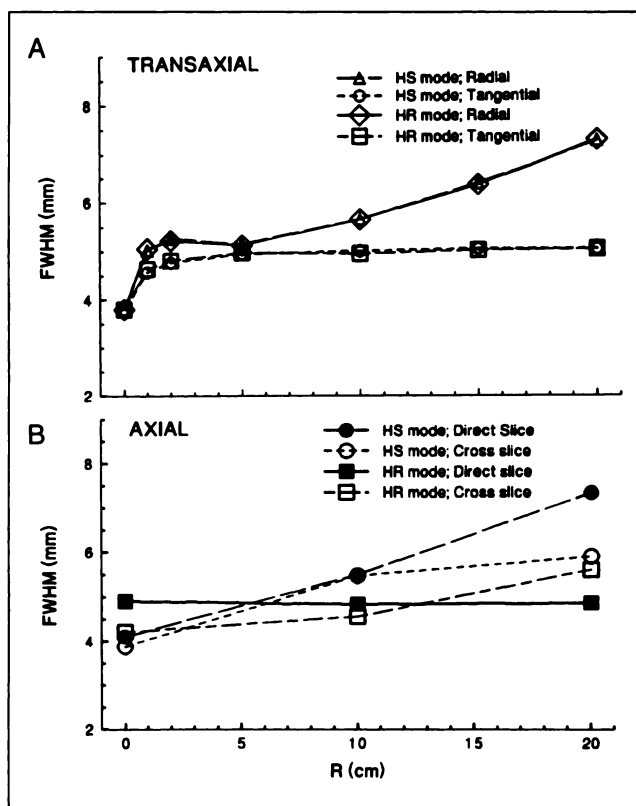
FIGURE 2. Transaxial resolution (A) and axial slice profile width (B) as a function of the distance from the center. Data were processed in the high-resolution (HR) and high-sensitivity (HS) modes of the PET scanner. The lower and upper gamma-energy discriminator settings are 300 keV and 650 keV, respectively.

was calculated from these values and the known radioactivity concentration in the phantom.

Imaging Studies

To demonstrate the transaxial resolution of the PET scanner, a micro-resolution phantom (Data Spectrum, Hillsborough, NC) was imaged. The phantom is a "cold rod" phantom 7.5 cm in diameter and consists of six segments of lucite rods within a background of ^{18}F-activity (~0.5 μCi/cc) in water. The diameters of the rods are equal in each segment, ranging from 1.2 mm to 4.8 mm. The center-to-center rod spacing is twice the diameter. The images were reconstructed using a ramp filter 4 mm wide, scatter correction and no attenuation correction.

Two characteristic two-dimensional image sets were acquired of the normal human brain: one 30 min after intravenous administration of 8.5 mCi of FDG for 20 min, another 20 sec after intravenous administration of 66 mCi of ^{15}O-water as a bolus for 1 min. Calculated attenuation correction was performed. A patient with a lung tumor was scanned for 20 min starting 30 min after intravenous administration of 10.2 mCi of FDG. A 20-min transmission scan was acquired before radiotracer injection to apply measured attenuation correction to the emission data.

RESULTS AND DISCUSSION

Intrinsic Spatial Resolution

The transaxial resolution of the PET scanner is shown in Figure 2. The transverse resolution (FWHM) in the radial

direction increases from 3.8 mm at the center to 7.3 mm at a radius of 20 cm. The FWHM in the tangential direction increases relatively slowly, reaching 5.0 mm at a radius of 20 cm. Transaxial resolution is equivalent for direct and cross slices and independent of the acquisition mode (high sensitivity or high resolution).

The axial resolution defined by the FWHM of the axial slice profile width is shown in Figure 2. For cross slices in the high-resolution mode, axial resolution degrades from 4.2 mm at the center to 5.6 mm at a radius of 20 cm. By contrast, axial resolution increases slightly from 4.9 mm at the center to 4.8 mm at a radius of 20 cm. In the high-sensitivity mode, the axial response profile width increases from ~4 mm at the center to 5.9 mm (cross slices) and 7.3 mm (direct slices) at a radius of 20 cm.

Spatial resolution did not change significantly when the LLD was decreased to 250 keV from the standard LLD of 300 keV (data not shown).

In the high-sensitivity mode of the PET scanner, the point-spread function is nearly isotropic for FOVs within a 10-cm radius, showing a FWHM near 5 mm. Thus, for brain studies, where reslicing of the data is common, minimal artifacts are introduced by the reorientation process. Body studies, however, would be affected to a minor degree by the poorer resolution at larger radii. Nevertheless, the intrinsic spacial resolution in all three directions never exceeds 7.4 mm FWHM within a 20-cm radius. These spatial resolution characteristics are consistent with the BGO crystal dimensions of 4.0 mm transaxial × 8.1 mm axial. By comparison, the PC-4096 PET scanner, which has BGO crystal dimensions 6 mm transaxial × 12 mm axial, shows a transaxial resolution of 5.9 mm FWHM at the center and an axial resolution of 6.0 mm FWHM for direct slices (11). These and other recent whole-body PET scanners based on BGO block detectors show a similar dependence of spatial resolution on detector size (2–4,11,12), confirming a formula suggested by Moses and Derenzo (13).

Scatter

The scatter distribution in the transverse plane for a line source in the center of the water-filled phantom is shown in Figure 3 for septa in and septa out. The scatter fraction, calculated from sinograms obtained at radii 0, 4 and 8 cm, is shown in Table 1 for three scanning modes and three LLD settings. The average scatter fraction is 8.1% (9.4%) and 8.7% (10.2%) for direct and cross slices in the high-resolution (high sensitivity) mode, respectively, at the standard LLD setting of 300 keV. A three- to fourfold increase in the scatter fraction is noted when the septa are retracted. A similar increase in scatter fraction with the removal of septa was reported for other scanners with retractable septa (3,4,14,15). In both two-dimensional and three-dimensional scanning modes, the scatter fraction increases slightly as the LLD setting is decreased from 350 to 250 keV (Table 1).

The accuracy of the two-dimensional scatter correction

technique was tested at an LLD of 300 keV. The radioactivity concentration indicated in a nonradioactive water-filled insert relative to the radioactive background was $-0.7\% \pm 1.3\%$ of the background over all 35 imaging planes, indicating the validity of the two-dimensional scatter correction implementation.

Sensitivity

Table 2 shows the true event sensitivity of the PET scanner as a function of scanning mode and LLD. For two-dimensional data acquired with an LLD of 300 keV, the cross slices are 76% more sensitive than the direct slices in the high-resolution mode; this difference is reduced to 13% in the high-sensitivity mode. The gain in sensitivity associated with scanning in the high-sensitivity mode relative to the high-resolution mode is 124% for direct slices, 43% for cross slices and 65% for the system as a whole. The true event sensitivity with septa out (1200 kcps/(μCi/cc) at LLD = 300 keV) is approximately fivefold higher than that of the two-dimensional high-sensitivity mode and ninefold higher than that of the high-resolution mode. System sensitivities are increased 12%–15% as the LLD is decreased from 350 to 250 keV.

These data are consistent with the high efficiency of BGO as detector material. Only slightly lower spatial resolution is attained in the high-sensitivity mode of the scanner relative to the high-resolution mode (Fig. 2). Thus, the significantly higher sensitivity of the high-sensitivity mode relative to the high-resolution mode strongly favors this acquisition mode for most, if not all, applications of PET imaging of the human body.

Count Rate Performance

Figure 4 shows the count rate performance characteristics of the PET scanner for two-dimensional scanning in the high-sensitivity mode at an LLD of 300 keV. Similar data are shown in Figure 5 for three-dimensional scanning. Indices of count rate performances at LLD settings of 250, 300 and 350 keV are shown
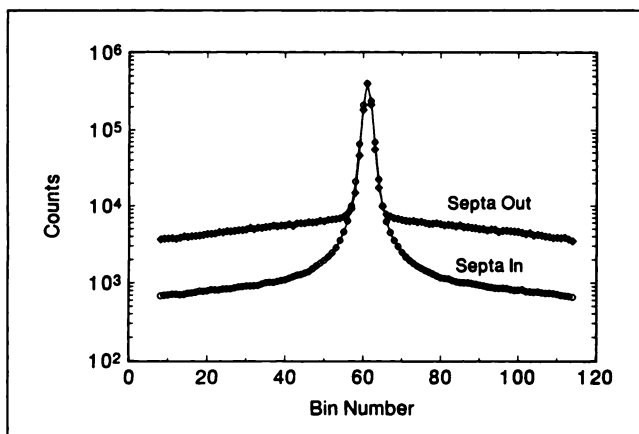
TABLE 1
Scatter Fraction (%) as a Function of Scanning Mode and Energy Setting

Scanning mode	Slice type	LLD (keV) 250	300	350
Septa in; high-resolution mode	Direct	8.7 ± 0.3	8.1 ± 0.3	7.4 ± 0.2
	Cross	9.3 ± 0.3	8.7 ± 0.3	7.9 ± 0.2
Septa in; high-sensitivity mode	Direct*	10.1 ± 0.3	9.4 ± 0.3	8.6 ± 0.2
	Cross*	10.9 ± 0.3	10.2 ± 0.2	9.2 ± 0.2
Septa out	n.a.	36.4	34.4	31.9

*Slices 1, 2, 34 and 35 are excluded.
The upper gamma-energy discriminator setting is 650 keV.

in Table 3. The noise equivalent count rate (NECR) is shown in Figure 6 as a function of radioactivity concentration for all scanning modes. A maximum NECR of 261 (180) kcps is reached at a radioactivity concentration of 4.1 (4.6) μCi/cc for the high-sensitivity (high resolution) mode. For both high-sensitivity and high-resolution scanning modes, the curves are very similar for LLDs between 250–350 keV (Fig. 6A). The insensitivity of NECR over this energy range demonstrates that increases in true event sensitivity obtained by lowering the LLD are nearly totally offset by increases in scatter and random coincidences.

Comparison of system-averaged NECR curves (Fig. 6B) shows this index to be higher for three-dimensional scanning than for two-dimensional scanning (high-sensitivity mode) at radioactivity concentrations under 1.0 μCi/cc. At radioactivity concentrations below 0.5 μCi/cc, the three-dimensional NECR is approximately threefold higher than the two-dimensional NECR. The maximum NECR for three-dimensional scanning is 39% lower than that of two-dimensional scanning, mainly due to a factor of four higher scatter event rate. Further evaluation of factors relating to image quality and quantitative accuracy (e.g., scatter correction) is necessary to compare more definitively the performance characteristics of two-dimensional and three-dimensional scanning.

The accuracy of the dead-time correction technique was tested by scanning the test phantom filled with ^{18}F in water. After reconstruction and ROI analysis through the user-interface, the dead-time corrected images indicated radioactivity concentration in the phantom with <3% error for radioactivity concentrations up to 6.6 μCi/cc (60% dead-time).

A comparison of count rate performance characteristics of this PET scanner to those of other scanners is of interest. Although dead-time characteristics (i.e., Table 3) or noise-equivalent count rates may be used for purposes of comparison, the applicability of such indices if derived solely from measurements with a standard homogeneous phantom may be limited to predict the practical utility of scanners in particular quantitative applications of PET. For example, the spatial and temporal dependences of dead-time losses for both myocardial and cerebral blood flow studies using a bolus of ^{15}O-water administration would be expected to behave differently than those of a static phantom study.

In addition, data are not generally available on the accuracy of applied dead-time correction techniques for specific applications. Furthermore, sensitivity characteristics should be compared

FIGURE 3. Average sinograms from a line source at the center of a water-filled performance phantom with septa in and out. Data were acquired with lower and upper gamma-energy discriminator settings of 300 keV and 650 keV, respectively.

TABLE 2
True Event Sensitivity (kcps/(μCi/cc)) as a Function of Scanning Mode and Energy Setting

Scanning mode	Slice type	LLD (keV)		
		250	300	350
Septa in; high-resolution mode	Direct	3.1 ± 0.3	2.9 ± 0.3	2.7 ± 0.3
	Cross	5.4 ± 0.3	5.1 ± 0.3	4.7 ± 0.3
	System total	146.8	138.2	128.5
Septa in; high-sensitivity mode	Direct*	6.9 ± 0.2	6.5 ± 0.2	6.0 ± 0.3
	Cross*	7.8 ± 0.2	7.3 ± 0.3	6.8 ± 0.3
	System total*	243.6	228.4	211.4
Septa out	System total	1266	1200	1127

*Slices 1, 2, 34 and 35 are excluded.
The upper gamma-energy discriminator setting is 650 keV.

along with a high count rate response, especially in applications where practical considerations (i.e., dosimetry) may place limits on the quantity of radiotracer allowed to be administered to the subject. Accordingly, we compared an index of dead-time losses (e.g., the radioactivity concentration in a 20-cm phantom at 50%

dead-time losses) together with the slice sensitivity normalized by slice thickness and expressed in units of cps · μCi^{-1} · ml · mm^{-1}.

The PET scanner showed 50% dead-time losses at a radioactivity concentration of 4.9 μCi/cc (Table 3) and a normalized (direct) slice sensitivity of 1529 (Table 2). A comparison of these indices to several recently developed BGO-based whole-body PET scanners shows this system to have a relatively good high count rate performance (3,4,11,12). For example, the PC-4096 PET scanner shows a higher radioactivity concentration of 8.6 μCi/cc at the 50% dead-time point (11). However, the higher value of this performance index can be partly attributed to (1) a lack of upper level gamma-energy discrimination of the PC-4096 allowing for acceptance of piled-up events, and (2) a lower sensi-
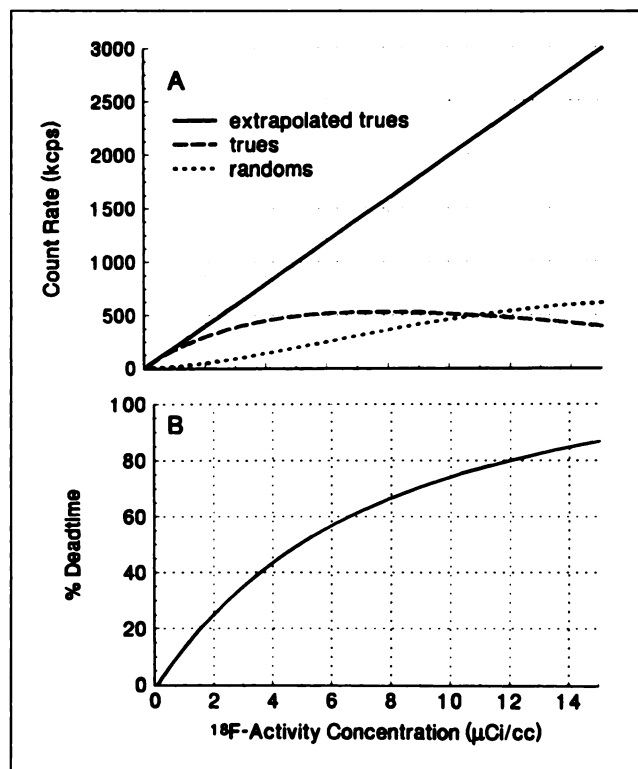

FIGURE 4. High count rate characteristics using a performance phantom filled with ^{18}F in water. The scanner is in the high-sensitivity mode (septa in) with lower and upper gamma-energy discriminator settings of 300 keV and 650 keV, respectively. In the upper figure (A), the true and random count rates are plotted for a 24-cm FOV. Also shown is the calculated true event as extrapolated from the true curve at low specific activities. In the lower figure (B), the percent dead-time is calculated from the ratio of measured trues + scatter-to-extrapolated trues + scatter.
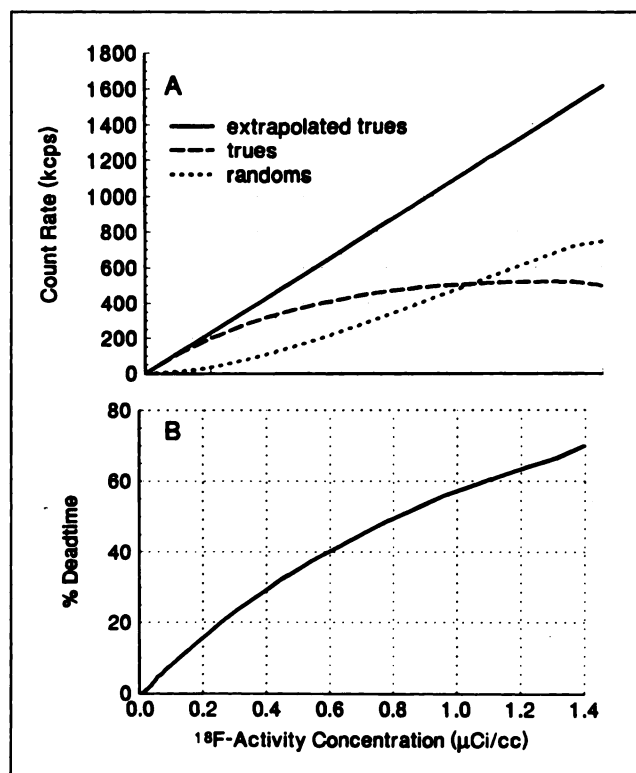

FIGURE 5. Same as in Figure 4, but with septa out.

TABLE 3
Indices of System Count Rate Performance

Scanning LLD		50% Dead-time point		Peak trues		Trues = randoms point	
Mode	(keV)	Activity density (μCi/cc)	Trues rate (kcps)	Activity density (μCi/cc)	Trues rate (kcps)	Activity density (μCi/cc)	Trues rate (kcps)
Septa in; high-resolution mode	250	4.87	316	7.21	341	12.33	298
	300	4.90	300	7.93	325	13.50	267
	350	4.86	281	7.64	305	14.60	230
Septa in; High-sensitivity mode	250	4.90	515	7.21	557	9.82	539
	300	4.92	489	7.93	531	10.87	499
	350	4.89	457	7.64	497	11.94	444
Septa out	250	0.81	502	1.10	533	0.85	510
	300	0.83	480	1.23	518	1.00	505
	350	0.82	454	1.29	492	1.16	490

The upper gamma-energy discriminator setting is 650 keV.

tivity of the PC-4096: its normalized sensitivity is about one-half that of the new system.

Temporal Resolution

Dynamic PET studies with high sampling rates may be useful to monitor rapid changes in the distribution of radioactivity in the body. With this system, the data transfer rate from histogram memory to the hard disk (~3 Mbyte/sec) imposes certain restrictions on frame acquisition rates. A maximum of 1 frame per second is achievable until the histogram memory is filled. In the present configuration of the system, the 128-Mbyte histogram memory will hold ~39 two-dimensional frames, beyond which the minimum frame duration is 2 sec. In the three-dimensional mode, the memory can hold only four frames. For dynamic three-dimensional studies having more than three frames, data transfer would require ~10 sec per frame. The amount of histogram memory in the system may be increased to a maximum of 512 Mbytes. With such a configuration, the memory could hold ~160 frames in the two-dimensional mode and 16 frames in the three-dimensional mode. Given the inverse relationship of frame rate and image count statistics in practice, the temporal resolution capabilities of the new PET scanner are adequate to perform any conceivable study in the two-dimensional mode, i.e., bolus ^{15}O-water blood flow studies. Yet, a mild limitation on frame acquisition rate (6 frames/min) may be imposed in three-dimensional studies in the present configuration of the system.

Imaging Studies

A two-dimensional image of a micro-resolution phantom is shown in Figure 7. Individual cold rods could be visualized against a hot background for rod diameters as low as 3.2 mm, consistent with the measured intrinsic transaxial resolution of the PET scanner.
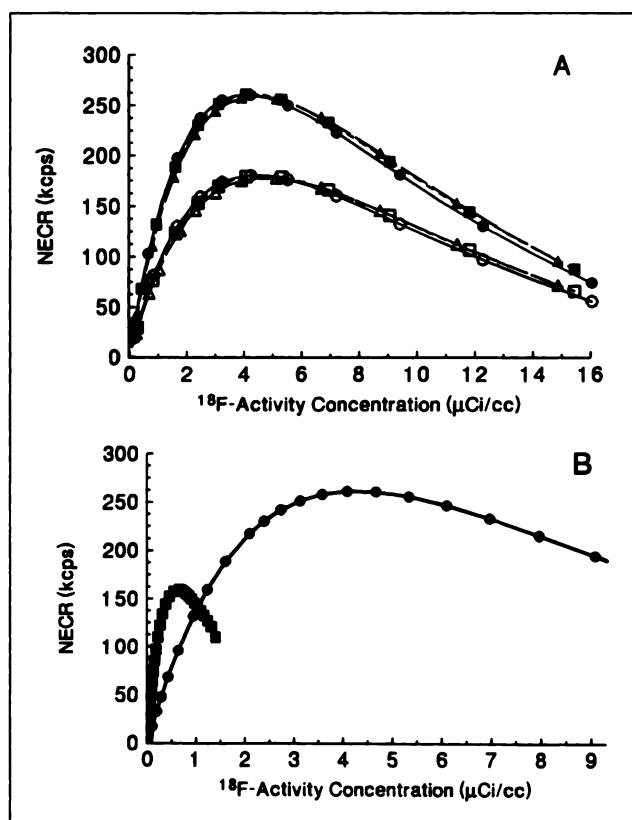
Images of FDG accumulation in normal human brain are

FIGURE 6. Comparison of system noise-equivalent count rate curves for (A) two-dimensional scanning high-resolution (open symbols) and high sensitivity modes (filled symbols); and (B) two-dimensional scanning in the high-sensitivity mode (circles) and three-dimensional scanning (squares). In the upper figure (A), the LLD is 250 keV (circles), 300 keV (squares) or 350 keV (triangles). The upper level discriminator setting is 650 keV. In the lower figure (B), the LLD is 300 keV for both scanning modes.
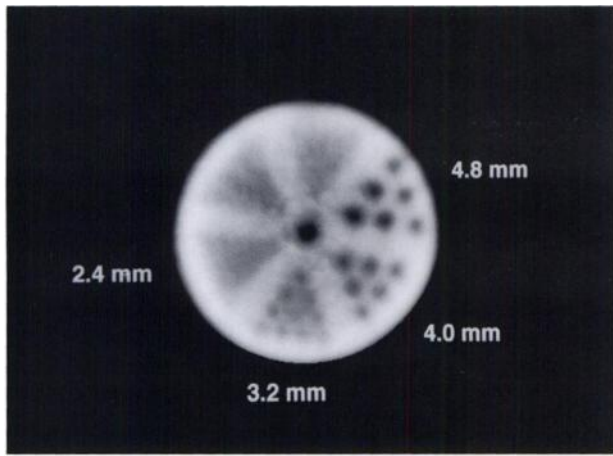
FIGURE 7. Image of the micro-resolution phantom acquired in the high-sensitivity mode. The cold lucite rods are discriminated from the hot background for rod diameters as low as 3.2 mm. The corresponding sinogram contains ~25 million counts.

FIGURE 9. Images of the accumulation of ^{15}O-water in a normal human brain. Scanning commenced 20 sec after intravenous injection of radiotracer (66 mCi) for 1 min. Calculated attenuation was applied. Six of 35 two-dimensional image planes are shown. There are at most 0.5 million counts represented in each image plane.

shown in Figure 8. The high spatial resolution of the PET scanner is demonstrated, for example, by visualization of the sulcal and gyral pattern of the cerebral cortex and delineation of brain structures including the anterior limb of the internal capsule. Images of the normal human brain after a bolus injection of ^{15}O-water (Fig. 9) are of lower quality than those with FDG, due to lower accumulated counts and higher positron energy resulting in a longer mean pathlength before annihilation. Nevertheless, small brain structures are visualized and good contrast is seen between grey and white matter.

Figure 10 shows FDG accumulation in the thorax of a patient having a lung tumor. The data from two contiguous axial FOVs were reformatted into coronal and sagittal projections (only the coronal are shown). This display, along with the transverse two-dimensional images, allows rapid localization of metabolically active neoplasms. The measurement of radioactivity concentration in the tumor (nCi/cc) provides a clinically useful index of neoplasm malignancy.

CONCLUSIONS

The newly developed whole-body PET scanner has high spatial resolution, temporal resolution, sensitivity and count rate performance. A set of test measurements using the SNM/NEMA guidelines has been presented. Clinical
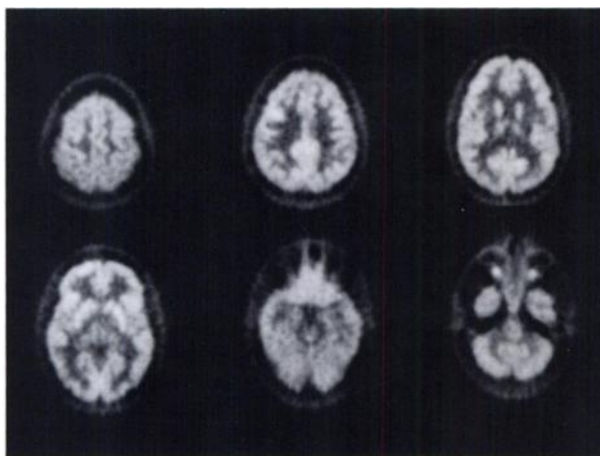

FIGURE 8. Images of the accumulation of FDG in a normal human brain. A 20-min scan was acquired 30 min after the intravenous injection of radiotracer (8.5 mCi). Calculated attenuation correction was applied. Six of 35 two-dimensional image planes are shown. There are at most 3 million counts represented in each image plane.
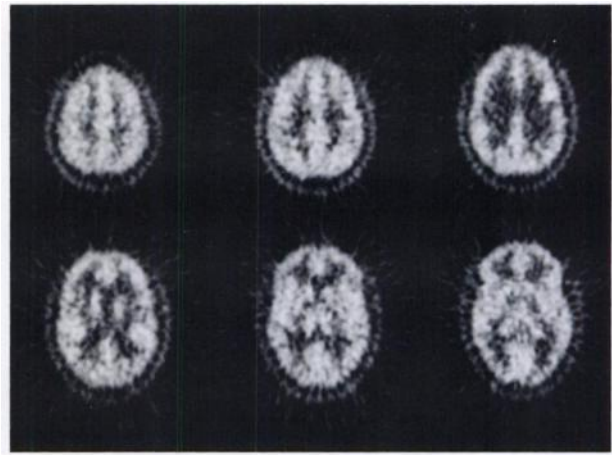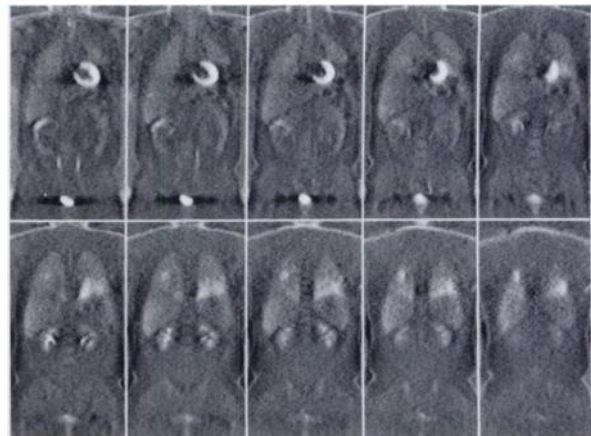

FIGURE 10. Coronal image projections (representing five contiguous axial FOVs) of a thorax of a patient with lung neoplasms. The emission data were acquired 30 min after intravenous administration of FDG (10.2 mCi). Measured attenuation correction was applied. Metabolically active tissue is indicated in posterior regions of both lungs. A nonlinear (approximately logarithmic) scaling of the image grey scale was found to be beneficial for differentiation of low uptake values in the presence of high uptakes in the heart and bladder.

images demonstrate the utility of the scanner in brain and body PET imaging applications. The scanner is well suited for both research and clinical applications of PET.

ACKNOWLEDGMENTS

REFERENCES

1. Ter-Pogossian MM, Phelps ME, Hoffman EJ, et al. A positron-emission transaxial tomograph for nuclear medicine imaging (PETT). *Radiology* 1975;114:89–98.
2. Koeppe RA, Hutchins GD. Instrumentation for positron emission tomography: tomographs and data processing and display systems. *Semin Nucl Med* 1992;22:162–181.
3. Wienhard K, Eriksson L, Grootoonk S, Casey M, Pietrzyk U, Heiss WD. Performance evaluation of the positron scanner ECAT EXACT. *J Comput Assist Tomogr* 1992;16:804–813.
4. Wienhard K, Dahlbom M, Eriksson L, et al. The ECAT EXACT high resolution: performance of a new high resolution positron scanner. *J Comput Assist Tomogr* 1994;18:110–118.
5. Mertens JD, Bhend WL. Digital coincidence detection: a scanning VLSI implementation. *Conference Record of the IEEE NSS/MIC*, Orlando, FL. 1992;879–881.
6. Huesman RH, Derenzo SE, Cahoon JA, et al. Orbiting transmission source for positron emission tomography. *IEEE Trans Nucl Sci* 1988;35:735–739.
7. Jones WF, Digby WM, Luk WK, Casey ME, Byars LG. Optimizing rod window width in positron emission tomography. *Conference Record of the IEEE NSS/MIC*. Orlando, FL. 1992;982–984.
8. Karp JS, Daube-Witherspoon ME, Hoffman EJ, et al. Performance standards in positron emission tomography. *J Nucl Med* 1991;32:2342–2350.
9. Bergström M, Eriksson L, Bohm C, Blomqvist G, Litton J. Correction for scattered radiation in a ring detector positron camera by integral transformation of the projections. *J Comput Assist Tomogr* 1983;7:42–50.
10. Strother SC, Casey ME, Hoffman EJ. Measuring PET scanner sensitivity: relating countrates to image signal-to-noise ratios using noise equivalent counts. *IEEE Trans Nucl Sci* 1990;37:783–788.
11. Rota-Kops E, Herzog H, Schmidt A, Holte S, Feinendegen LE. Performance characteristics of an eight-ring whole-body PET scanner. *J Comput Assist Tomogr* 1990;14:437–445.
12. Mullani NA, Gould KL, Hitchens RE, et al. Design and performance of POSICAM 6.5 BGO positron camera. *J Nucl Med* 1990;31:610–616.
13. Moses WW, Derenzo SE. Empirical observation of resolution degradation in positron emission tomographs utilizing block detectors [Abstract]. *J Nucl Med* 1993;34:101P.
14. Cherry SR, Dahlbom M, Hoffman EJ. Three-dimensional PET using a conventional multislice tomograph without septa. *J Comput Assist Tomogr* 1991;15:655–668.
15. Townsend DW, Geissbuhler A, Defrise M, et al. Fully three-dimensional reconstruction for a PET camera with retractable septa. *IEEE Trans Med Imag* 1991;10:505–512.